GSA DATA REPOSITORY 2014369

Temperature and leaf wax δ^2H records demonstrate seasonal and regional controls on Asian monsoon proxies

Elizabeth K. Thomas, Steven C. Clemens, Warren L. Prell, Timothy D. Herbert, Yongsong Huang, Zhengyu Liu, Jaap S. Sinninghe Damsté, Youbin Sun, Xinyu Wen

Materials and Methods

1. Lipid biomarker extraction and purification.

255 samples were obtained from ODP Site 1146, Holes B and C, for organics analysis. Free lipids were extracted from freeze-dried samples (ca. 9 to 24 g dry weight) with an Accelerated Solvent Extractor 200 (Dionex) using dichloromethane (DCM):methanol 19:1 (v:v). The samples were split volumetrically, reserving 10% of the total lipid extract (TLE) for alkenone analysis. The remaining TLE was prepared for *n*-alkanoic acid and GDGT analysis following previously published methods (Thomas et al., 2012; Kim et al., 2010). First, the TLEs were separated on solid phase Aminopropyl silica gel flash columns using DCM:methanol 1:1 (v:v) as the neutral eluent and 4% acetic acid in diethyl ether as the acid eluent. All flash column separations used three column volumes of each eluent, unless otherwise stated. The acid fraction was then methylated in anhydrous 5% HCl in methanol at 60°C overnight. Hydroxyl-carboxylic acids were removed from the methylated acid fractions using silica gel flash columns with DCM as the eluent, after eluting apolar compounds with hexane. The GDGTs were purified on an aluminum oxide flash column using DCM:methanol 1:1 (v:v) as the eluent, after eluting apolar and ketone fractions with hexane:DCM 9:1 (v:v) and hexane:DCM 1:1 (v:v; four column volumes), respectively. The polar fractions were dissolved in hexane:isopropanol 99:1 (v:v), and filtered through a 0.4 μm PTFE filter.

2. Alkenone analysis.

An aliquot of each extract was analyzed for alkenones ($U^{K'}_{37}$) by gas chromatography at Brown University, using standard published methodology (Herbert et al., 1998). Sea surface temperatures were calculated using the global core-top calibration, with a standard error of ±1.5°C (Müller et al., 1998). Laboratory analytical error, 0.2°C (1σ), was calculated based on a composite sediment standard, which is extracted and analyzed

every 3 months. The pooled standard deviation for these analyses, calculated using replicate analyses of individual extracts, is 0.07°C (1σ).

3. Hydrogen isotope analysis.

The hydrogen isotope ratio of the C_{28} fatty acid methyl ester (FAME) was determined using gas chromatography-pyrolysis-isotope ratio mass spectrometry at Brown University using previously described methods (Thomas et al., 2012). Isotope values are expressed in per mille (‰) relative to Vienna Standard Mean Ocean Water (VSMOW). The pooled standard deviation for these analyses, calculated using the results of triplicate analyses of each extract, is 1.6‰ (1σ). Analysis of an external FAME standard consisting of C_{16}, C_{18} ,C_{22}, C_{24}, and C_{26} FAMES, injected twice after every sixth sample injection, had an analytical error of 2‰ (1σ). The measured FAME δ^2H values were corrected for the isotopic contribution of the three hydrogens in the methyl group added during methylation using the formula: $\delta^2H_{wax} = [(2n + 2) \times \delta^2H_{measured} + 123.7‰ \times 3]/(2n - 1)$ where n is the number of carbons in the molecule and -123.7‰ is the δ^2H value for the added methyl group.

4. TEX^H_{86} temperature analysis.

GDGTs were analyzed at the Royal Netherlands Institute for Sea Research, using previously described methods (Kim et al., 2010). Sea surface temperatures were calculated using the TEX^H_{86} calibration, with a standard error of ±2.5°C(Kim et al., 2010). The pooled standard deviation for these analyses, calculated using replicate analyses of individual extracts, is 0.3°C (1σ).

5. Precipitation source regions.

We determined precipitation source regions for the Pearl River catchment (24.0°N, 110.0°E; Fig. 1) using HYbrid Single-Particle Lagrangian Integrated Trajectory (HYSPLIT) analysis of NCEP-NCAR Reanalysis data from 2007-2011 (Kalnay et al., 1996; Draxler and Hess, 1998). We backtracked airmasses at twelve-hour timesteps for seven days from a point 500 m above ground level at the study site. We then subsampled this dataset to include only airmass trajectories that resulted in precipitation within twelve hours of arriving at the study site and grouped the trajectories by month (Fig. 1).

6. Community Climate System Model Version 3: Isotope-enabled transient simulation.

We simulated continuous climate evolution of the past 21,000 years (Liu et al., 2009) in a state-of-the-art coupled ocean-atmosphere model, the Community Climate System Model version 3 (CCSM3, T31 resolution) of the National Center for Atmospheric Research (hereafter TRACE simulation) (Yeager et al., 2006). The simulation is forced by realistic

external forcing of insolation, atmospheric greenhouse gases, melt water fluxes and continental ice sheets (Liu et al., 2009). To explicitly compare model results with precipitation isotope observations, we further simulated the evolution of atmospheric water isotopes ($\delta^{18}O$ only) using the isotope-enabled atmospheric component model of the CCSM3 CAM3 (T31 resolution) that incorporates fractionation associated with surface evaporation and cloud processes (Noone and Sturm, 2010). We performed 23 isotope snapshot sensitivity experiments in the last 21,000 years using the same CAM3 setup as in the TRACE experiment: 21 experiments are 1000 years apart, at 20 ka, 19 ka,…., 0 ka, and 2 additional experiments around the times of the Bølling-Allerød warming (14.5 ka) and the Younger Dryas (12.1 ka). Each experiment is forced by the same external forcing as for the TRACE experiment, and additionally, by a 50-year history of monthly SST and sea ice from the TRACE experiment. Surface ocean $\delta^{18}O$ values are prescribed as $\delta^{18}O = 1.6‰$ at the Last Glacial Maximum based on (Schrag et al., 1996), and are scaled to other time periods using the global benthic $\delta^{18}O$ stack. The mean of the last 40 years in each snapshot experiment is used for cross-snapshot analysis. The mean climate of each snapshot is similar to that of the TRACE simulation at the corresponding time. The prescribed ocean surface $\delta^{18}O$ boundary condition should not introduce large error because of the modest variation of $\delta^{18}O$ values over the surface ocean. Therefore, the oxygen isotopes simulated in the snapshot experiments can be considered a good representation of that simulated in the transient TRACE experiment, were the isotopes fully implemented into the coupled model. The evolution of the model $\delta^{18}O_p$ over China captures the major features of the cave $\delta^{18}O_{cave}$ records, albeit with a somewhat smaller magnitude (Liu et al., 2014).

7. Removing the effect of local condensation temperature from δ^2H_{wax} and $\delta^{18}O_{cave}$.
The effect of vapor transport history on precipitation δ^2H and $\delta^{18}O$ dominates the modern monthly data in southern China, whereas temperature does not exert a strong influence on the seasonal cycle of precipitation isotope variability in this region (Johnson and Ingram, 2004). In contrast, annual mean temperature and amount-weighted precipitation $\delta^{18}O$ at all GNIP stations in the Pearl River catchment are positively correlated (IAEA/WMO, 2011), with similar slopes obtained using the CCSM3 isotope-enabled simulation (Fig. DR1). Annual mean values are most representative of δ^2H_{wax} preserved at Site 1146, since leaf waxes are produced year-round in the Pearl River catchment. It is important to note that annual total precipitation amount has a weak linear relationship with annual weighted mean $\delta^{18}O_p$ in the GNIP data for the pearl River catchment, and is in the opposite sense of the "amount effect" (depleted $\delta^{18}O_p$ corresponds to less precipitation; Fig. DR1; IAEA/WMO, 2011). The precipitation amount-$\delta^{18}O_p$ relationship in the CCSM3 data is also weak, but in the correct sense of the "amount effect". Furthermore,

thermodynamic principles demonstrate that at temperatures >0°C, condensing water becomes enriched in ^2H by >1‰ for each 1°C increase (Majoube, 1971). The combination of thermodynamics, modern empirical data, and model precipitation isotope data suggest that temperature has an important influence on annually-integrated precipitation isotopes in the Pearl River catchment.

Paleoclimate model simulations suggest that orbital-scale temperature change (i.e., from the Last Glacial Maximum 20,000 years ago to present) is on the order of 2.5 to 5.0°C in the South China Sea and the Pearl River catchment (Fig. DR1; Jiang et al., 2011). This is similar to the orbital-scale temperature change that we reconstruct in the northern South China Sea (Fig. 2). Sea surface temperature in the northern South China Sea covaries with air temperature in the Pearl River catchment (Fig. DR1; Kalnay et al., 1996; Jiang et al., 2011), so we used our South China Sea surface temperature records as a proxy for surface air temperature in the Pearl River catchment. Paleoclimate model simulations suggest that temperature change is comparable in these two regions (Fig. DR1; Jiang et al., 2011). Due to a more continental climate (i.e., greater temperature variability) in the western Pearl River catchment, the amplitude of glacial-interglacial scale temperature change may be greater in the Pearl River catchment than in the northern South China Sea. Thus, temperature variability in the South China Sea underestimates temperature variability in the Pearl River catchment, and the effects of temperature estimated by our calculations are therefore conservative.

We used the following steps to remove the effect of temperature from δ^2H_{wax}, propagating error where appropriate (Fig. 2C):

1. Convert temperature-$\delta^{18}O_p$ to temperature-δ^2H_p by multiplying by 8 (3.7±0.5‰ $°C^{-1}$) (Rozanski et al., 1993).
2. Calculate ΔT for each $U^{K'}_{37}$-based SST relative to average Holocene SST at Site 1146 (25°C).
3. Convert ΔT to $\Delta\delta^2H$ using the temperature-δ^2H_p relationship.
4. Subtract $\Delta\delta^2H$ from δ^2H_{wax} to yield a δ^2H_{wax} record with the effects of local condensation temperature removed ($\delta^2H_{wax\text{-}T}$; Fig. 2).

We propagate error through the temperature removal calculations as follows (steps correspond to steps above):

1. Multiply the slope error bar by 8 as well (Rozanski et al., 1993)
2. No error propagation necessary

3. Propagate calibration error of SST value (1.5°C and 2.5°C for $U^{K'}_{37}$ and TEX^{H}_{86}, respectively) and error of temperature-δ^2H_p slope from the CCSM3 model.
4. Propagate error of replicate δ^2H_{wax} measurements.

Removing the effect of ice volume from δ^2H_{wax} and $\delta^2H_{wax\text{-}T}$ has a negligible impact on the amplitude of each record. The precession-band phases change slightly (Table DR1), but within error of the original records, and therefore does not influence our results or conclusions.

For the sake of consistent treatment of the leaf wax and speleothem proxies, we also experimented with removing the temperature effect from $\delta^{18}O_{cave}$. For this purpose, we used the $U^{K'}_{37}$-inferred sea surface temperature record from ODP Site 1146 because no millennial-scale Pleistocene terrestrial temperature record currently exists in the immediate vicinity of the caves. Over orbital and glacial-interglacial time scales, we expect the timing of temperature change to be similar throughout southeastern China, although the magnitude may be different. To our knowledge, there are no published temperature reconstructions in the cave region with appropriate time span and resolution. Removing the effect of condensation temperature from $\delta^{18}O_{cave}$ changes the phase at the precession band by only 6°, which does not change our conclusions (Figs. 3, DR2, DR3). This small effect is due to the fact that the precession-band phasing of SST is more similar to $\delta^{18}O_{cave}$ than to δ^2H_{wax}, and addition of two similar-phase vectors results in a vector with a similar phase (Fig. 3). Moreover, temperature-dependent oxygen isotope fractionation associated with water vapor condensation and calcite precipitation have opposite signs (Majoube, 1971; O'Neil et al., 1969), potentially reducing the effect of temperature variability in $\delta^{18}O_{cave}$.

8. Spectral Analysis.

Power spectra, coherency, and phase of 1146 time series and $\delta^{18}O_{cave}$ are presented in Fig. DR3. We used the Arand software package (Howell et al., 2006) to run these analyses. We calculated ETP by normalizing and averaging the three orbital parameters eccentricity, obliquity (tilt) and precession (June 21 perihelion; Laskar et al., 2004). Benthic foraminifera $\delta^{18}O$, raw δ^2H_{wax}, and temperature records show concentrations of variance at the eccentricity (100 kyr), and to a lesser extent at the obliquity (41 kyr) and precession (23 kyr) bands (Fig. DR3). $\delta^2H_{wax\text{-}T}$ and planktonic foraminifera $\delta^{18}O$ show strong variance at the eccentricity and precession bands, whereas $\delta^{18}O_{cave}$ shows a strong variance only at the precession band (Fig. DR3).

We applied Gaussian band-pass filters to the precipitation isotope records, (δ^2H_{wax}, $\delta^2H_{wax\text{-}T}$, $\delta^{18}O_{cave}$, and $\delta^{18}O_{cave\text{-}T}$) to extract oscillations associated with the precession period. The Gaussian band-pass filter was centered at 0.044 kyr^{-1} (22.7 kyr period) with a bandwidth of 0.01 (18.5-29.4 kyr period). The results are shown in Figs. 2, DR2, and DR3, and Table DR1.

Source of Leaf Waxes to ODP Site 1146

Analyses of grain size distribution for glacial and interglacial sediments in the northern South China Sea indicate that dust is a minor source of sediments to this region (Boulay et al., 2005; Boulay et al., 2007). Thus, fluvial input dominates terrestrial influx. Clay mineral distributions and neodymium and strontium isotope measurements indicate that the primary source of fluvial material to the northern South China Sea during both glacial and interglacial periods is the Pearl River (Boulay et al., 2008). In the Ganges-Brahmaputra rivers, a monsoonal system similar to the Pearl River, leaf waxes are integrated from throughout the catchment, proportional to the suspended sediment load of individual tributaries (Galy et al., 2011). This could lead to some bias towards tributaries with higher suspended sediment load, but overall, we infer that the primary source of leaf waxes to ODP Site 1146 is the Pearl River catchment.

N-alkanoic acids may be retained in the Pearl River for some period of time before being carried to our study site, thus potentially affecting the timing of the paleoclimate signal preserved in ODP Site 1146 sediments. Of the river catchments studied for leaf wax residence time, the Ganges River catchment is the most similar to the Pearl River catchment in latitude, climate, and seasonality. Estimates of *n*-alkanoic acid residence time for the Ganges River catchment range from 0.05 to 1.3 kyr, with a median residence time of 550 years (Galy and Eglinton, 2011). Assuming that these results could also apply to Pleistocene-age sediments in the Pearl River catchment, it is likely that leaf waxes are deposited at ODP Site 1146 on the order of 550 years after they are produced. This is half the time of our average sampling resolution, and therefore has a minimal impact on our results and conclusions. Even so, we conducted a sensitivity analysis to determine whether residence time would impact our precession-band phase results (Fig. 3). To do so, we assume that leaf waxes are 550 yr older than alkenones and GDGTs in the same sample, and subtract 550 yr from the leaf wax age prior to accounting for the effects of condensation temperature on δ^2H_{wax}. The precession-band phase of the resulting $\delta^2H_{wax\text{-}T}$ is in phase with P_{min}, within error (Fig. 3). Thus, leaf wax residence time does not affect our results or conclusions.

Growing Season Length and Leaf Wax Production

Satellite-based phenology studies suggest that plants grow year-round in southern China (Piao et al., 2006). Plants in moist subtropical forests continuously produce new leaves, with a small increase in leaf production during months with >100 mm precipitation (April to October; Fig. 1; Jackson, 1978). Because most phenology studies focus on regions that have marked plant leaf-out and senescence cycles (i.e. temperate regions), we obtained further confirmation of SE China growing season length using modern rainfed crop data from the Condensed Crop Calendar MIRCA2000 dataset (Portmann et al., 2010). We used only rainfed crops since their growing seasons are likely most representative of natural ecosystems. The dataset contains information for start and end of cropping periods, in months, of 26 individual crops, grouped by Chinese province. We calculated the number of months that crops are growing using only non-zero crop areas of non-permanent crops (crop numbers 1-11, 13, 15-17, 21, 26). We disregarded winter crops of wheat, rye, barley, and rapeseed, since these lie dormant during the winter (Portmann et al., 2010). These data demonstrate that the growing season is 10-12 months long in the Pearl River catchment (Fig. 1A).

Table DR1. Phase and coherency of Asian paleoclimate records relative to P_{min}

Record	Precession Phase (°)	Phase Error (°)	Coherency
	(-) = lead		
In Figure 3:	(+) = lag		
$U_K^{37'}$ SST (cold)	97	4	0.989[b]
δ^2H_{wax}[a]	51	10	0.969[c]
$\delta^2H_{wax\text{-}T}$ ($U_K^{37'}$) Hysplit-Syntrace[a]	7	12	0.950[c]
$\delta^{18}O_{ben}$ (Min. Ice Vol.)[a]	-52	6	0.988[b]
$\delta^{18}O_{ben}$ (Max. Ice Vol.)	128	6	0.988[b]
$\delta^{18}O_{plank}$[a]	-46	2	0.999[b]
$\delta^{18}O_{cave}$[a]	-43	4	0.994[b]
$\delta^{18}O_{cave\text{-}T}$ ($U_K^{37'}$) Hysplit-Syntrace[a]	-48	4	0.995[b]
Gulang Loess Grain Size	127	13	0.946[c]
Other ODP 1146 records:			
TEX_{86}^H SST (cold)	108	6	0.985[b]
Other orbital-scale Asian paleoclimate records:			
Gulang Loess Magnetic Susceptibility	-37	16	0.920[c]
Arabian Sea Summer Monsoon Stack (Clemens and Prell, 2007)	-98	13	0.941[c]
Arabian Sea Summer Monsoon Stack (Caley et al., 2011)	-119	13	0.954[c]
Heqing lake Summer Monsoon Stack (An et al., 2011)	-100	52	0.500
Other temperature-δ^2H relationships and ice volume correction:			
$\delta^2H_{wax\text{-}T}$ ($U_K^{37'}$) Thermodynamic[a]	38	11	0.958[c]
$\delta^2H_{wax\text{-}T}$ ($U_K^{37'}$) Modern China GNIP[a]	32	12	0.954[c]
$\delta^2H_{wax\text{-}T}$ ($U_K^{37'}$) Modern Global GNIP[a]	-32	9	0.974[c]
$\delta^2H_{wax\text{-}T}$ (TEX_{86}^H) Hysplit-Syntrace[a]	11	11	0.961[c]
$\delta^2H_{wax\text{-Ice Volume}}$[a]	41	16	0.920[c]
$\delta^2H_{wax\text{-Ice Volume \& T}}$[a]	-7	18	0.896

[a]Multiplied by -1 prior to calculating phase.
[b]Coherent at 95% level.
[c]Coherent at 80% level.

Figure DR1. CCSM3 transient simulation and GNIP temperature, precipitation, and precipitation $\delta^{18}O$ data in SE China. **A.** Mean annual air temperature vs. annual weighted mean precipitation $\delta^{18}O$ in the Pearl River catchment for five time slices in the CCSM3 simulation (colored dots) and for modern GNIP data (stations at Guangzhou, Guilin, Hong Kong, Kunming, and Liuzhou; IAEA/WMO, 2011). Linear regression equations and Pearson correlation coefficients shown for each time slice in corresponding color. GNIP and model data yield similar temperature-precipitation $\delta^{18}O$ relationships. **B.** Same as A. but for total annual precipitation vs. annual weighted mean precipitation $\delta^{18}O$. GNIP and model data do not yield similar precipitation amount-precipitation $\delta^{18}O$ relationships. **C.** Slope of temperature-precipitation $\delta^{18}O$ relationship (shown in A.) for all 23 CCSM3 time slices vs. age. The slope of the temperature-precipitation $\delta^{18}O$ relationship increases through time. Modern GNIP data has a slope of 0.4‰ $°C^{-1}$ (red star), similar to late Holocene values obtained in the CCSM3 simulation. **D.** Surface temperature for 23 1-kyr time slices in the Pearl River catchment (101-116°E, 24°N) compared to surface temperature in the South China Sea (112-116°E, 20°N). Surface temperature in the Pearl River catchment is ca. 10°C cooler than in the South China Sea. The temperature range in both regions is similar on these time scales, so ΔSST in the South China Sea is a reasonable proxy for Δ mean annual air temperature in the Pearl River catchment.

Figure DR2. $\delta^{2}H_{wax}$ and $\delta^{18}O_{cave}$ records with and without the effect of condensation temperature removed. **A.** $\delta^{2}H_{wax\text{-}T}$ using $U^{K'}_{37}$-based SST (red), and $\delta^{2}H_{wax\text{-}T}$ using TEX^{H}_{86}-inferred SST (orange). Error bars as in Figure 2. **B.** Raw $\delta^{18}O_{cave}$ (black; Wang et al., 2008; Wang et al., 2001; Cheng et al., 2009) and $\delta^{18}O_{cave\text{-}T}$ (blue). $\delta^{18}O_{cave\text{-}T}$ calculated by downscaling $\delta^{18}O_{cave}$ and ODP Site 1146 SST to 1 kyr resolution, and then following steps described for calculating $\delta^{2}H_{wax\text{-}T}$. **C.** Precession-filtered $\delta^{18}O_{cave}$ (black) and $\delta^{18}O_{cave\text{-}T}$ (blue; Supplementary Information text) plotted against orbital precession (gray dashed curve; Laskar et al., 2004). The amplitude modulation increases slightly for $\delta^{18}O_{cave\text{-}T}$, but the phase is unchanged, within error. $\delta^{18}O_{cave}$ has been converted to VSMOW scale for ease of comparison with $\delta^{2}H_{wax}$. **D.** Precession-filtered $\delta^{2}H_{wax\text{-}T}$ ($U^{K'}_{37}$, red; TEX^{H}_{86}, orange; Supplementary Information text) plotted against orbital precession as in C. The amplitude modulation is slightly larger for $\delta^{2}H_{wax\text{-}T}$ calculated using TEX^{H}_{86}, but the phase is unchanged. **E.** ODP Site 1146 benthic foraminifera $\delta^{18}O$ (Caballero-Gill et al., 2012).

Figure DR3. Spectral analysis results for ODP Site 1146 and Chinese speleothem records. Isotope records were multiplied by -1 so that depleted isotopes were compared to maximum NH summer insolation at the precession band. Spectral density (on a log scale) of paleoclimate records (red) compared to orbital forcing (eccentricity-tilt-precession, ETP; blue; we define P_{min}, June 21 perihelion, as zero phase; Laskar et al., 2004), including coherency and phase. Dashed lines show the 80 and 95% confidence intervals. Error bars on phasing shown only for orbital frequencies. All panels show time series compared to ETP except panels F, G, and L, which show ODP Site 1146 $\delta^2H_{wax\text{-}T}$ ($U^{K'}_{37}$) compared to $\delta^{18}O_{cave\text{-}T}$, ODP Site 1146 $\delta^{18}O_{ben}$ compared to $\delta^{18}O_{cave\text{-}T}$, and ODP Site 1146 δ^2H_{wax} compared to ODP Site 1146 $U^{K'}_{37}$-inferred SST.

Figure DR4. Comparison of multiple sea surface temperature reconstructions at ODP Site 1146. **A.** Scatter plot of $U^{K'}_{37}$- and TEX^{H}_{86}-inferred SST. TEX^{H}_{86}-inferred SST is consistently 1°C warmer than $U^{K'}_{37}$-inferred SST, a difference that is within calibration error for the two proxies (Kim et al., 2010; Müller et al., 1998). The high correlation coefficient indicates that the two records contain similar trends and variability. **B.** Time series of $U^{K'}_{37}$-inferred SST, TEX^{H}_{86}-inferred SST, and foraminifera transfer function SST (Huang et al., 2005), all from ODP Site 1146 cores. The foraminifera data yield seasonal temperature estimates, and indicate that most of the temperature amplitude occurs during the winter. The lipid biomarker SST proxies, which are calibrated to mean annual temperature, yield records with similar timing to the foraminifera SST. The lipid biomarker SST proxies have amplitudes similar to foraminifera-inferred winter SST. The similarity between these three independent temperature proxies indicates that they provide reliable temperature reconstructions at this site.

Figure DR5. January vector winds at 850 mbar over Asia at 20 ka (max. ice volume) and 8 ka (min. ice volume) in the CCSM3 transient simulation (Liu et al., 2009). **A.** Maps of winds at the two time slices. Red star = Site 1146; Yellow dots = Sanbao & Linzhu and Hulu caves. Arrows denote wind direction, arrow length and color denote wind strength. Red lines indicate the boundary between Pacific and westerly moisture near the east coast of Asia. **B.** Zonal average 850 mbar winds. Solid line is zonal average over Asia (40-130°E), dashed line is zonal average over the entire globe. Whereas global average Northern Hemisphere westerlies (ca. 30 to 60°N) were stronger and shifted south at 20 ka, westerlies over land in Asia were the same strength at 20 and 8 ka, but covered a wider latitudinal band at 8 ka. The wider band of westerlies at 8 ka pushed Pacific-derived northeasterly winds ca. 10° longitude offshore. **C.** Difference

between monthly simulated precipitation amount (colored bars) and $\delta^{18}O_p$ (white boxes) for 20 ka and 8 ka in central China (28-32°N, 109-120°E). Positive values indicate that winter months at 20 ka were wetter with more enriched $\delta^{18}O_p$ than at 8 ka. These data support our hypothesis that moist, isotopically enriched Pacific airmasses contributed more precipitation to central China when ice volume was large and the winter westerly winds were more meridionally confined.

Data Repository References

An, Z., Clemens, S.C., Shen, J., Qiang, X., Jin, Z., Sun, Y., Prell, W.L., Luo, J., Wang, S., and Xu, H., 2011, Glacial-interglacial Indian summer monsoon dynamics: Science, v. 333, no. 6043, p. 719–723.

Boulay, S., Colin, C., and Trentesaux, A., 2008, Traceurs sédimentaires des variations du niveau marin et de la mousson sud-est asiatique depuis 450ka en mer de Chine du Sud: Comptes Rendus Geoscience, v. 340, no. 6, p. 367–378, doi: 10.1016/j.crte.2008.03.002.

Boulay, S., Colin, C., Trentesaux, A., Clain, S., Liu, Z., and Lauer-Leredde, C., 2007, Sedimentary responses to the Pleistocene climatic variations recorded in the South China Sea: Quaternary Research, v. 68, no. 1, p. 162–172, doi: 10.1016/j.yqres.2007.03.004.

Boulay, S., Colin, C., Trentesaux, A., Frank, N., and Liu, Z., 2005, Sediment sources and East Asian monsoon intensity over the last 450 ky. Mineralogical and geochemical investigations on South China Sea sediments: Palaeogeography, Palaeoclimatology, Palaeoecology, v. 228, no. 3, p. 260–277.

Caballero-Gill, R.P., Clemens, S.C., and Prell, W.L., 2012, Direct correlation of Chinese speleothem $\delta^{18}O$ and South China Sea planktonic $\delta^{18}O$: Transferring a speleothem chronology to the benthic marine chronology: Paleoceanography, v. 27, no. 2, doi: 10.1029/2011PA002268.

Caley, T., Malaizé, B., Zaragosi, S., Rossignol, L., Bourget, J., Eynaud, F., Martinez, P., Giraudeau, J., Charlier, K., and Ellouz-Zimmermann, N., 2011, New Arabian Sea records help decipher orbital timing of Indo-Asian monsoon: Earth and Planetary Science Letters, v. 308, no. 3–4, p. 433–444, doi: 10.1016/j.epsl.2011.06.019.

Cheng, H., Edwards, R.L., Broecker, W.S., Denton, G.H., Kong, X., Wang, Y., Zhang, R., and Wang, X., 2009, Ice Age Terminations: Science, v. 326, no. 5950, p. 248–252, doi: 10.1126/science.1177840.

Clemens, S.C., and Prell, W.L., 2007, The timing of orbital-scale Indian monsoon changes: Quaternary Science Reviews, v. 26, no. 3, p. 275–278.

Draxler, R.R., and Hess, G.D., 1998, An overview of the HYSPLIT_4 modelling system for trajectories, dispersion and deposition: Australian Meteorological Magazine, v. 47, no. 4, p. 295–308.

Galy, V., and Eglinton, T., 2011, Protracted storage of biospheric carbon in the Ganges-Brahmaputra basin: Nature Geoscience, v. 4, no. 12, p. 843–847, doi: 10.1038/ngeo1293.

Galy, V., Eglinton, T., France-Lanord, C., and Sylva, S., 2011, The provenance of vegetation and environmental signatures encoded in vascular plant biomarkers carried by the Ganges–Brahmaputra rivers: Earth and Planetary Science Letters, v. 304, no. 1-2, p. 1–12, doi: 10.1016/j.epsl.2011.02.003.

Herbert, T.D., Schuffert, J.D., Thomas, D., Lange, C., Weinheimer, A., Peleo-Alampay, A., and Herguera, J.C., 1998, Depth and seasonality of alkenone production along the California margin inferred from a core top transect: Paleoceanography, v. 13, no. 3, p. 263–271.

Howell, P., Pisias, N., Ballance, J., Baughman, J., and Ochs, L., 2006, ARAND Time-Series Analysis Software: Brown University, Providence, RI.

Huang, B., Jian, Z., and Wang, P., 2005, Paleoceanographic evolution recorded in the northern South China Sea since 4 Ma: Science in China Series D, v. 48, no. 12, p. 2166–2173, doi: 10.1360/03yd0564.

IAEA/WMO, 2011, Global Network of Isotopes in Precipitation. The GNIP Database.:.

Jackson, J.F., 1978, Seasonality of Flowering and Leaf-Fall in a Brazilian Subtropical Lower Montane Moist Forest: Biotropica, v. 10, no. 1, p. 38–42, doi: 10.2307/2388103.

Jiang, D., Lang, X., Tian, Z., and Guo, D., 2011, Last glacial maximum climate over China from PMIP simulations: Palaeogeography, Palaeoclimatology, Palaeoecology, v. 309, no. 3-4, p. 347–357, doi: 10.1016/j.palaeo.2011.07.003.

Johnson, K.R., and Ingram, B.L., 2004, Spatial and temporal variability in the stable isotope systematics of modern precipitation in China: implications for paleoclimate reconstructions: Earth and Planetary Science Letters, v. 220, no. 3–4, p. 365–377, doi: 10.1016/S0012-821X(04)00036-6.

Kalnay, E., Kanamitsu, M., Kistler, R., Collins, W., Deaven, D., Gandin, L., Iredell, M., Saha, S., White, G., Woollen, J., Zhu, Y., Leetmaa, A., Reynolds, R., Chelliah, M., et al., 1996, The NCEP/NCAR 40-Year Reanalysis Project: Bulletin of the American Meteorological Society, v. 77, no. 3, p. 437–471, doi: 10.1175/1520-0477.

Kim, J.-H., van der Meer, J., Schouten, S., Helmke, P., Willmott, V., Sangiorgi, F., Koç, N., Hopmans, E.C., and Damsté, J.S.S., 2010, New indices and calibrations derived from the distribution of crenarchaeal isoprenoid tetraether lipids: Implications for past sea surface temperature reconstructions: Geochimica et Cosmochimica Acta, v. 74, no. 16, p. 4639–4654, doi: 10.1016/j.gca.2010.05.027.

Laskar, J., Robutel, P., Joutel, F., Gastineau, M., Correia, A.C.M., and Levrard, B., 2004, A long-term numerical solution for the insolation quantities of the Earth: Astronomy and Astrophysics, v. 428, no. 1, p. 261–285, doi: 10.1051/0004-6361:20041335.

Liu, Z., Otto-Bliesner, B.L., He, F., Brady, E.C., Tomas, R., Clark, P.U., Carlson, A.E., Lynch-Stieglitz, J., Curry, W., Brook, E., Erickson, D., Jacob, R., Kutzbach, J., and Cheng, J., 2009, Transient simulation of last deglaciation with a new mechanism for Bolling-Allerod warming: Science, v. 325, no. 5938, p. 310–314, doi: 10.1126/science.1171041.

Liu, Z., Wen, X., Brady, E.C., Otto-Bliesner, B., Yu, G., Lu, H., Cheng, H., Wang, Y., Zheng, W., Ding, Y., Edwards, R.L., Cheng, J., Liu, W., and Yang, H., 2014, Chinese cave records and the East Asia Summer Monsoon: Quaternary Science Reviews, v. 83, p. 115–128, doi: 10.1016/j.quascirev.2013.10.021.

Majoube, M., 1971, Fractionnement en oxygène-18 et en deutérium entre l'eau et sa vapeur.: Journal de chimie physique, v. 68, p. 1423–1436.

Müller, P.J., Kirst, G., Ruhland, G., Von Storch, I., and Rosell-Melé, A., 1998, Calibration of the alkenone paleotemperature index $U^{K'}_{37}$ based on core-tops from the eastern South Atlantic and the global ocean (60 N-60 S): Geochimica et Cosmochimica Acta, v. 62, no. 10, p. 1757–1772.

Noone, D., and Sturm, C., 2010, Comprehensive Dynamical Models of Global and Regional Water Isotope Distributions, *in* West, J.B., Bowen, G.J., Dawson, T.E., and Tu, K.P. eds., Isoscapes, Springer Netherlands, p. 195–219.

O'Neil, J.R., Clayton, R.N., and Mayeda, T.K., 1969, Oxygen Isotope Fractionation in Divalent Metal Carbonates: The Journal of Chemical Physics, v. 51, no. 12, p. 5547–5558, doi: doi:10.1063/1.1671982.

Piao, S., Fang, J., Zhou, L., Ciais, P., and Zhu, B., 2006, Variations in satellite-derived phenology in China's temperate vegetation: Global Change Biology, v. 12, no. 4, p. 672–685, doi: 10.1111/j.1365-2486.2006.01123.x.

Portmann, F.T., Siebert, S., and Döll, P., 2010, MIRCA2000—Global monthly irrigated and rainfed crop areas around the year 2000: A new high-resolution data set for agricultural and hydrological modeling: Global Biogeochemical Cycles, v. 24, no. 1, doi: 10.1029/2008GB003435.

Rozanski, K., Araguás-Araguás, L., and Gonfiantini, R., 1993, Isotopic patterns in modern global precipitation: Geophysical Monograph Series, v. 78, p. 1–36, doi: 10.1029/GM078p0001.

Schrag, D.P., Hampt, G., and Murray, D.W., 1996, Pore fluid constraints on the temperature and oxygen isotopic composition of the glacial ocean: Science, v. 272, no. 5270, p. 1930–1932, doi: 10.1126/science.272.5270.1930.

Thomas, E., McGrane, S., Jason Briner, and Huang, Y., 2012, Leaf wax δ^2H and varve-thickness climate proxies from proglacial lake sediments, Baffin Island, Arctic Canada: Journal of Paleolimnology, v. 48, no. 1, p. 193–207, doi: 10.1007/s10933-012-9584-7.

Wang, Y.J., Cheng, H., Edwards, R.L., An, Z.S., Wu, J.Y., Shen, C.-C., and Dorale, J.A., 2001, A High-Resolution Absolute-Dated Late Pleistocene Monsoon Record from Hulu Cave, China: Science, v. 294, no. 5550, p. 2345–2348, doi: 10.1126/science.1064618.

Wang, Y., Cheng, H., Edwards, R.L., Kong, X., Shao, X., Chen, S., Wu, J., Jiang, X., Wang, X., and An, Z., 2008, Millennial- and orbital-scale changes in the East Asian monsoon over the past 224,000 years: Nature, v. 451, no. 7182, p. 1090–1093, doi: 10.1038/nature06692.

Yeager, S.G., Shields, C.A., Large, W.G., and Hack, J.J., 2006, The Low-Resolution CCSM3: Journal of Climate, v. 19, no. 11, p. 2545–2566, doi: 10.1175/JCLI3744.1.

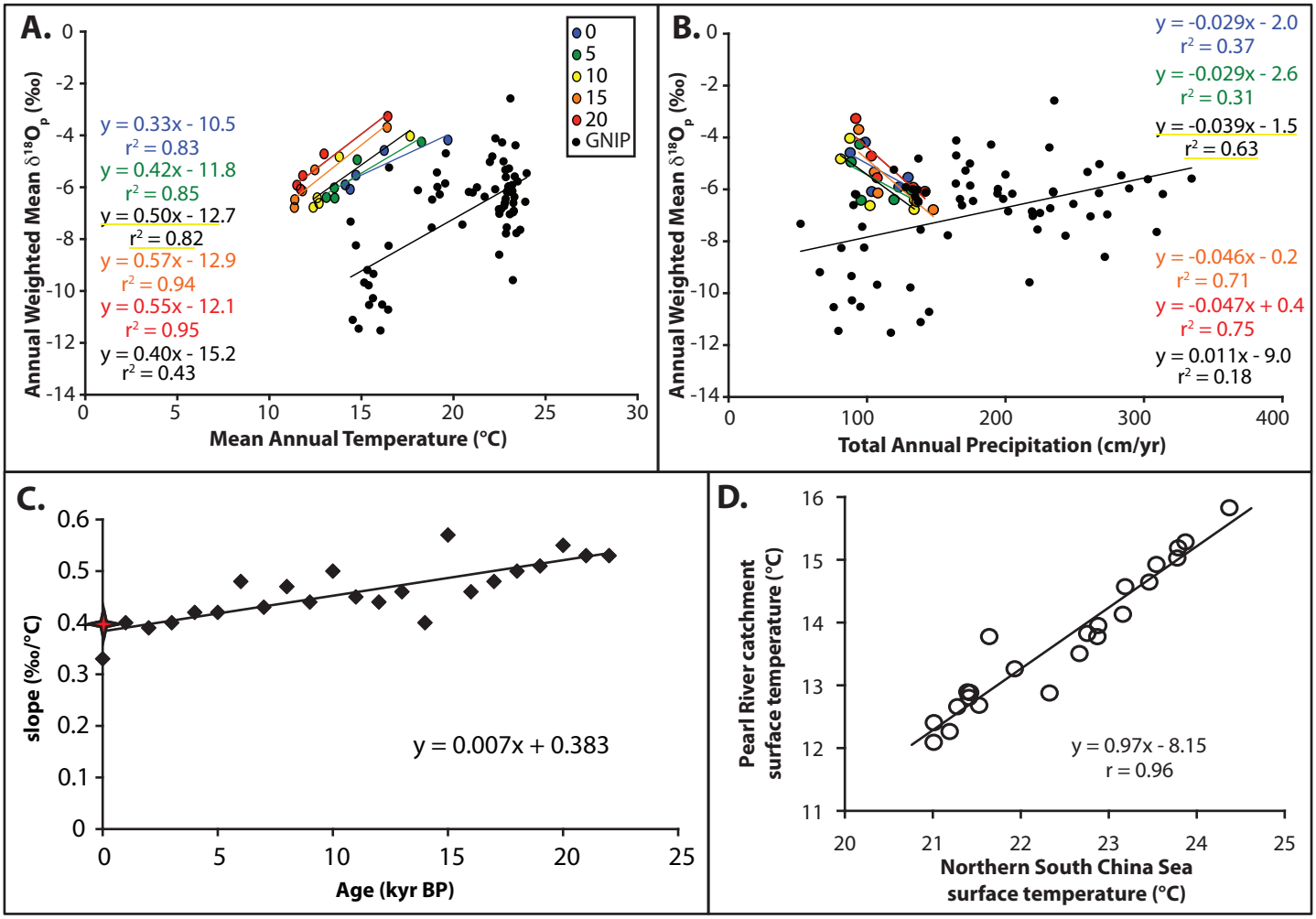

Thomas et al., Fig. DR1

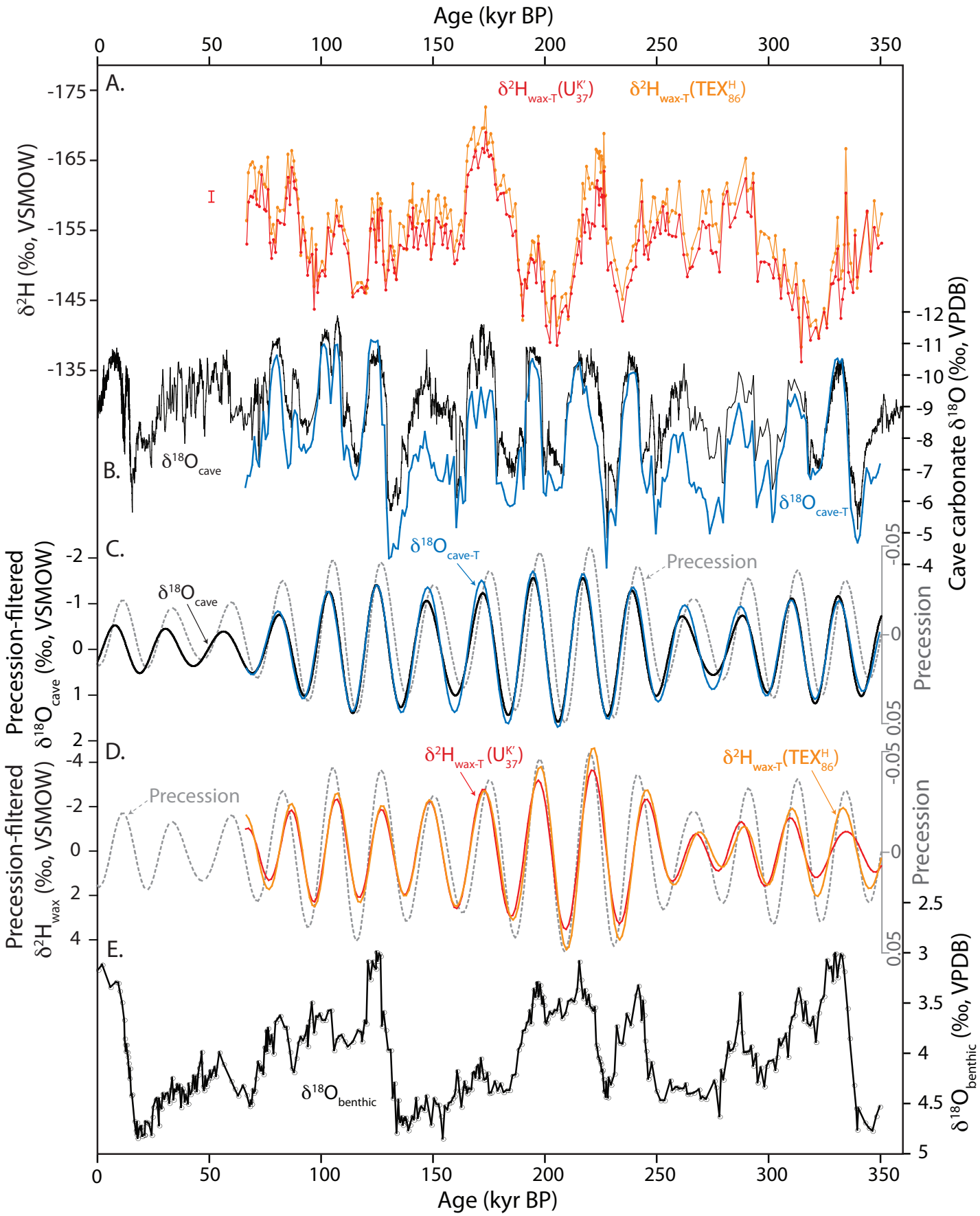

Thomas et al. DR2

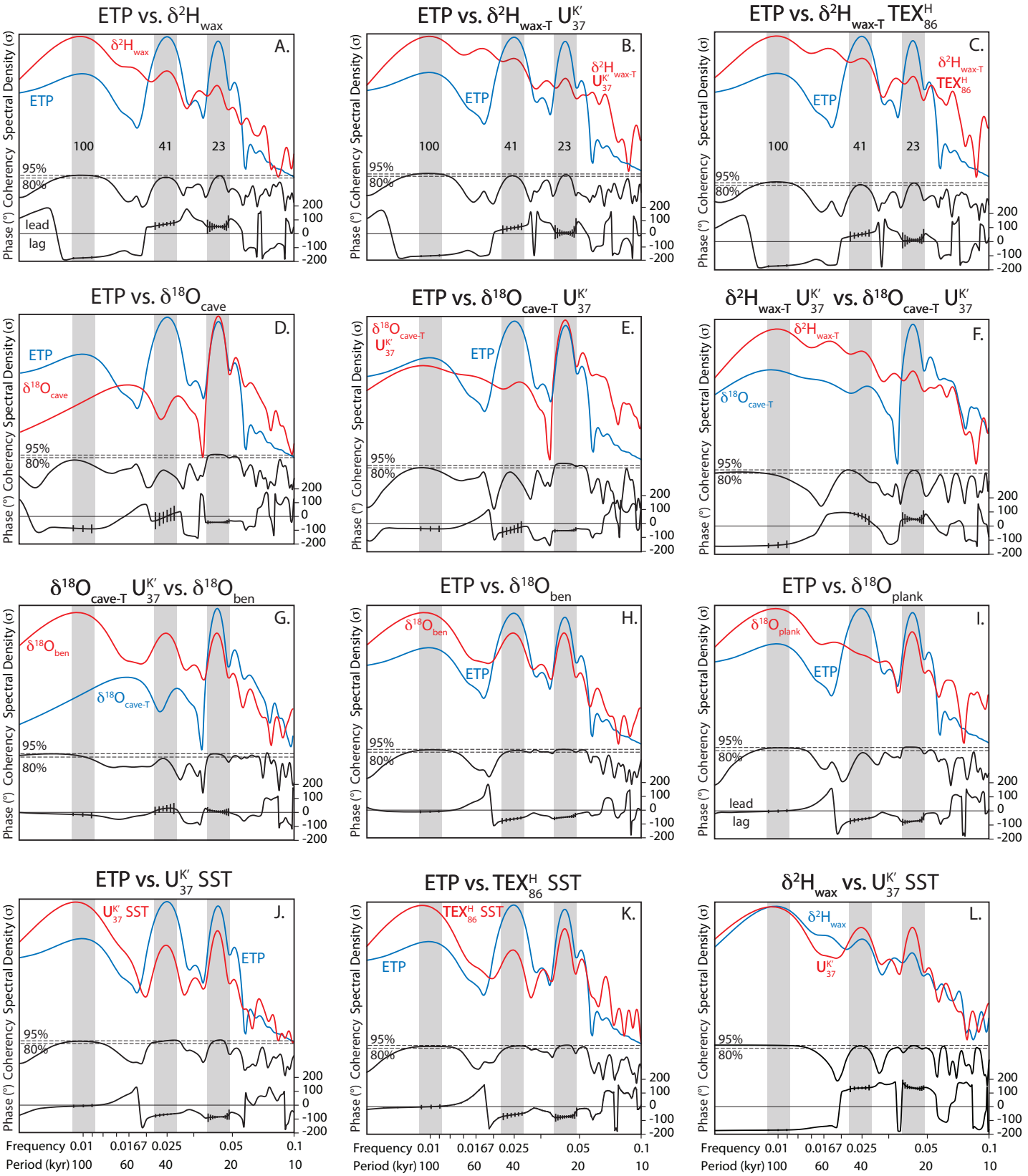

Thomas et al. DR3

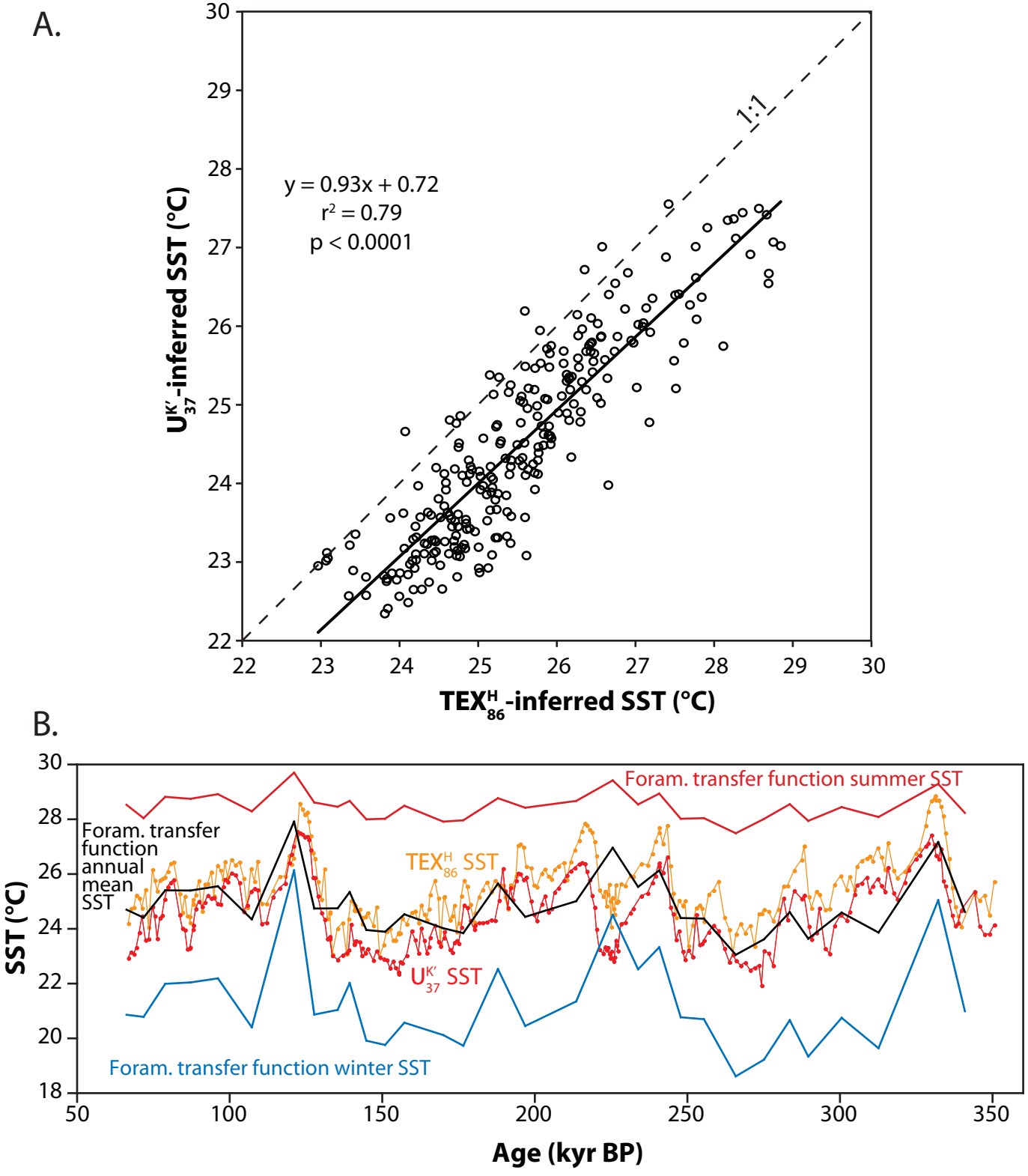

Thomas et al. DR4

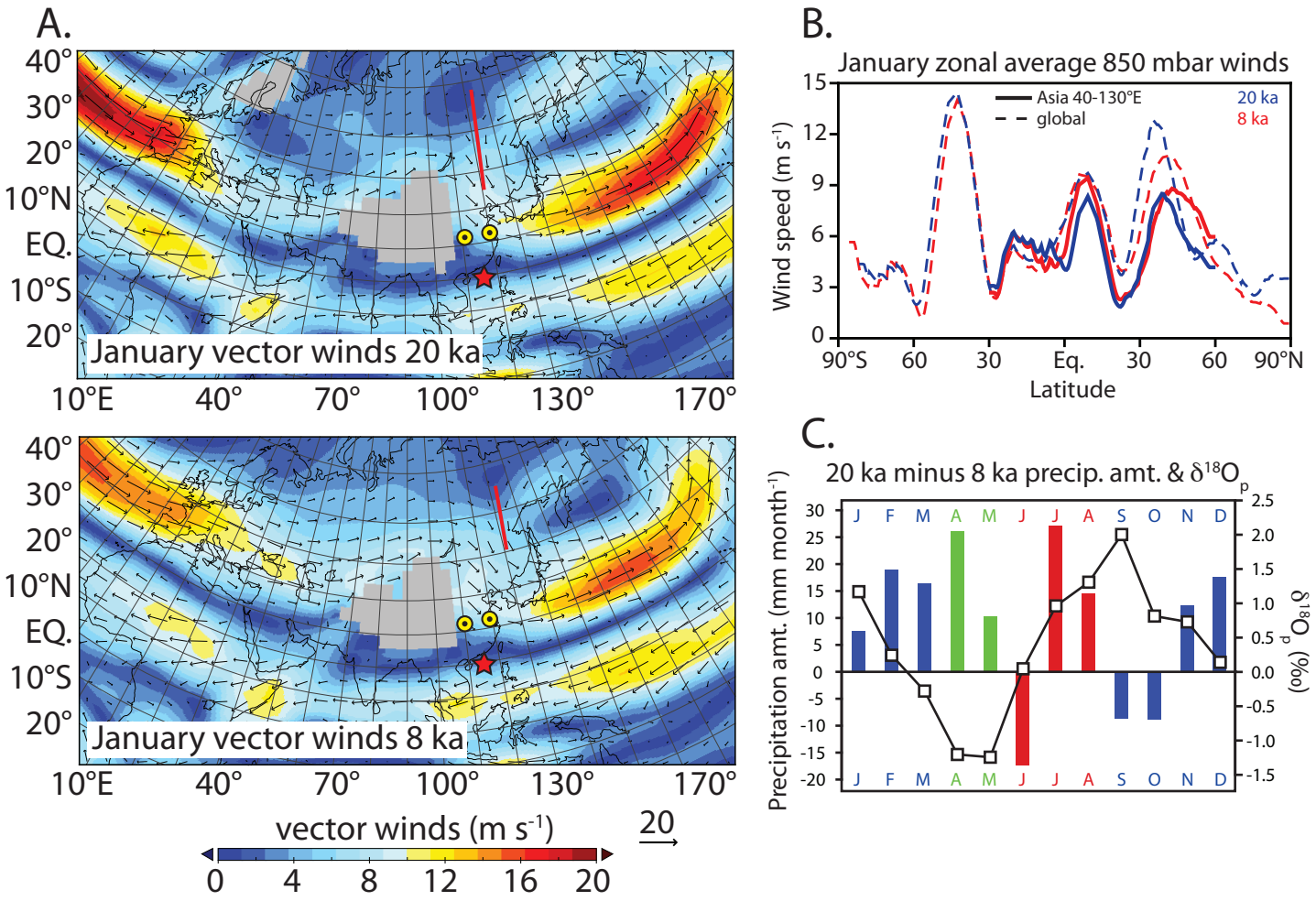

Thomas et al. Fig. DR5